An analysis on nanovoid growth in body-centered cubic single crystalline vanadium

S.Z. Xu [a,*], Z.M. Hao [a], Y.Q. Su [b], Y. Yu [a], Q. Wan [a], W.J. Hu [a]

[a] Institute of Structural Mechanics, China Academy of Engineering Physics, 621900 Mianyang, PR China
[b] School of Earth and Space Sciences, University of Science and Technology of China, 230026 Hefei, PR China

ARTICLE INFO

ABSTRACT

Molecular dynamics simulations were performed to analyze nanovoid growth in single crystalline vanadium under tension. Radial distribution function at the first nearest neighbor distance was calculated to find out the critical strain rate below which the deformation of specimen was static. Then a tensile stress was exerted on both void contained box and intact box under two constraint conditions. Homogenous dislocations were nucleated in intact box at yield point; while for void contained box with void radius twice the lattice constant, $\langle 111 \rangle \{110\}$ shear loops were punched out from void surface. The formation of shear loops was the result of the splitting of purely screw cores on three non-planar planes, as well as their transformations to more stable two-fold non-planar dislocations under tension. The asymmetry of loops was influenced by both strain rate and triaxiality of system. It is also found that, in lower rate cases the yield point and peak stress point coincided; however, the two points separated at higher rate due to the inadequate void growth rate. Mean square displacement of void surface atoms were given out to geometrically depict the void evolution. Moreover, simulations with different initial porosity and box size were performed respectively. It is shown that when void reduced to contain only one vacancy, dislocations can be nucleated independently of the void; when porosity was large enough, the interactions between void and its periodic images were noticeable. Also, when both the void and box were large, triangular prismatic loops on $\{110\}$ planes were observed at void surface, which may be contributed to a combined effect of the intersection of shear loops and the ledges along the void surface. Finally, the results of our MD simulations agreed well with that from Lubarda equation.

© 2011 Elsevier B.V. All rights reserved.

1. Introduction

The nucleation and growth of nanovoid play an important role in failure of ductile metals [1]. Under tensile loading, void nucleates initially at weak points of material such as the grain boundary [2]. Then void dilates due to the need to relax internal stress, minimizing the associated elastic energy in the system; meanwhile, void transforms into an irregular shape under the localization of shear stress, e.g., an initial spherical void will become nonspherical, even under all-around uniform far-field tension [3]. Eventually, void will either interact with adjoining ones before coalescence [4], or collapse into a crack [5], both of which are known as the primary causes of failure of ductile metals. Such processes and relevant nanomechanisms have been investigated extensively in the last few decades [6–9].

Most of the early works on void growth were continuum treatments, some of which were focused on physically valid damage function [10–12], where the mass transport was taken as the void growth mechanism [13,14]. It was due to the development of molecular dynamics (MD) methods that the void growth of nanoscale can be analyzed more thoroughly. To the authors' knowledge, Belak [15] was the first person who studied the nucleation and growth of nanovoids in single crystalline and polycrystalline metal at high strain rate using large-scale MD simulation. This work, along with others of LLNL [2,16–20], showed that the growth of spherical voids occur through anisotropic dislocation nucleation and emission. Moreover, regardless of the orientation of the simulation cell, voids in FCC lattice grow with octahedral shape, which is in agreement with the shape of the growing voids observed experimentally by Stevens et al. [21]. In addition, a laser-driven shock experiment conducted by Lubarda et al. [22] showed that void growth can not be accomplished by vacancy diffusion alone, even when the shock heating is taken into account. They proposed two dislocation-emission-based mechanisms for void growth—prismatic loop and shear loop. After emitted, the loops intersect across each other at junctions, making materials stronger [19]. These mechanisms have been verified by other works [23,24]. Recently, Lubarda [25] extended his own theory to nanovoids growth under combined loading.

Much has been learnt about the ductile fracture through nanovoid growth. Except the studies on nanomechanisms, some more methodology-type influences on single void growth under static

* Corresponding author. Tel.: +86 15883770742; fax: +86 816 2281485.
 E-mail address: shuozhixu@gmail.com (S.Z. Xu).

deformation can be categorized into several factors: strain rate [2], loading pattern [26], initial porosity and void volume growth [27], initial void shape and shape change [17], specimen size [20], lattice orientation [28–30], etc. Recent works were also devoted to analyze the shock-induced void collapse [31–33], void–void interaction and coalescence [18,34], void–dislocation interaction [35–39], void evolution and vacancy emission under irradiation [40,41]. Compared with void evolution in FCC lattice, there are much fewer discussions on that in BCC case due to the higher Peierls barrier for dislocation motion in BCC metal, leading to its tendency to twinning at high rate deformation and its character that the loops are formed from perfect dislocations rather than partials spanned by stacking fault ribbons in FCC lattice [20,42]. Also, the breakdown of Schmid law, which has been known to be the result of a combined effect of the shear stresses parallel and perpendicular to the Burgers vector [43,44], makes the void growth for BCC lattice more complicated. The contributions by Marians et al. [45], Rudd [20] and Tang et al. [46] represent the most significant efforts to reveal the growth and collapse of nanovoids in BCC monocrystals.

In the present study, we will discuss the effects of strain rate, specimen size, constraint condition and initial porosity on void evolution in BCC single crystalline vanadium, whose alloys are considered to be among the candidate materials for nuclear fusion application, where the microstructural evolution is very important [47–50]. Although all of these factors have been examined in void growth independently as mentioned above, none have really studied all of them together, particularly for BCC vanadium. Another reason we choose these factors is that the first three ones are significant even in intact specimen, see Refs. [51–53] for strain rate effects, Refs. [54,55] for specimen size effects and Refs. [56,57] for influences of boundary and constraint conditions. We investigated the void growth in pure vanadium at the atomic level here, so as to provide a first step forwards the comprehensive analysis of vanadium alloys.

This paper is organized as follows. It started in Section 2 with an overview of the MEAM potential, strain controlled MD method, atomic stress, critical strain rate, highlight of dislocations and void surface, as well as mean square displacement of void surface atoms. Detailed parameters used in this paper were also listed. In Section 3.1, both the void contained box and intact box were expanded at different rates under two constraint conditions. The stress–strain response, Poisson ratio, void volume growth and dislocation loops pattern were analyzed. Then specimens with various void sizes, from the smallest one containing only one vacancy to one that was large enough to interact with its neighboring images, were investigated in Section 3.2. In Section 3.3, the yield stress of specimens of different sizes but with uniform porosity were studied, and compared with the model presented by Lubarda et al. [22]. The conclusions were summarized in Section 4.

2. Simulation methodology

2.1. MEAM potential

In MD simulation, atoms interact with each other via empirical or semi-empirical potential; by Newton's law and equations of motion, new positions and velocities of atoms after a certain time step can be calculated. Thus, the accuracy of MD simulation relies very much on the reliability of potential, which depicts the forces between atoms. The embedded-atom method (EAM) of Daw and Baskes [58], which is based on density functional theory, has been successfully applied to FCC or nearly filled d-band transition metals and their alloys. However, some BCC transition metals have non-filled d-band, leading to directional bonding when adjacent atoms

overlap, which disagrees with the premise of isotropic electron cloud in EAM theory. Since BCC vanadium, also one of the transition metal series, has an electron configuration of $[Ar]3d^34s^2$, EAM potential will fail to be applicable. Based on EAM, the modified embedded-atom method (MEAM) presented by Baskes [59], takes angular forces into account, and is now one of the most widely used methods describing forces among atoms in a large variety of materials [60]:

$$\sum_i E_i = \frac{1}{Z_i} \sum_{j(\neq i)} E_i^u(R_{ij}) + \left[F_i(\bar{\rho}_i(R_{ij})/Z_i) - \frac{1}{Z_i} \sum_{j(\neq i)} F_i(\bar{\rho}_i^0(R_{ij})/Z_i) \right] \quad (1)$$

where the first term of the right side is the average of the energy per atom in the reference lattice at the first nearest neighbor (1NN) distance; the second term the difference between the actual embedding energy and the average embedding energy in the reference lattice at 1NN distance. The vanadium MEAM potential employed in this paper is due to Baskes [59], and its reliability, of calculating lattice parameter, elastic constants, cohesive energy, vacancy formation energy and surface energy, has been examined carefully by the authors. The calculations of Satou et al. [47] also showed that the elastic constants computed by this MEAM potential are more accurate than several vanadium EAM potentials.

2.2. MD simulation and atomic stress

A parallel molecular dynamics code LAMMPS [61] was used to deform the single crystal model. The classical equations of motion were integrated using Verlet algorithm with time step of 1 fs. The simulation cell is a 3-D single crystal BCC lattice in a cubic box with {1 0 0} faces. The lattice constant of BCC vanadium a_0 is 3.03686 Å. A certain number of atoms were removed to create a spherical void in the middle. Periodic boundary conditions were applied on all three directions in order to simulate a periodic array of voids in an infinite system. After the energy minimization, a Nose–Hoover thermostat [62,63] was applied for 10 ps to obtain the initial temperature of 10 K and the pressure of 0 Pa.

A remote tension was then exerted along x axis at a constant temperature of 10 K, which is quite low compared with that of 300 K employed in most previous works of nanovoid growth [2,17,20,26–30,45,46]. At 10 K, the deformation behavior of BCC vanadium is principally controlled by screw dislocations with non-planar cores [64–69], which will play a significant role in the loops pattern as will be discussed in Section 3.1. The strain-controlled simulations were realized by Parrinello–Rahman method [70]. Each time the box size was changed, all atoms were re-mapped to the new box, during which the coordinates of atoms were multiplied by a diagonal scaling matrix to get the new positions. Note that the velocities of atoms were not altered, i.e., it was not their new velocities that expanded the box, but an affine transformation of the positions of atoms which exactly matched the box deformation.

Though there are no free boundaries in the system apart from the void, two constraint conditions were applied: free transverse stress condition and fully constraint condition. In the first condition, the edges in y and z axes can shrink freely to make transverse stress vanish; in another condition, the Poisson effect is not allowed, so the transverse stress will increase as the box is expanded along x axis. These two conditions have been used by Kitamura et al. [57]. In our simulations, the free transverse stress condition is referred as 1-D stress condition, while the other 1-D strain condition, as shown in Fig. 1.

The definition of atomic level stress was originally presented as the virial formulation by Clausius [71], and was summarized by Born et al. [72]. However, Zhou et al. [73] have shown that the virial stress is not equivalent to the continuum measure of Cauchy
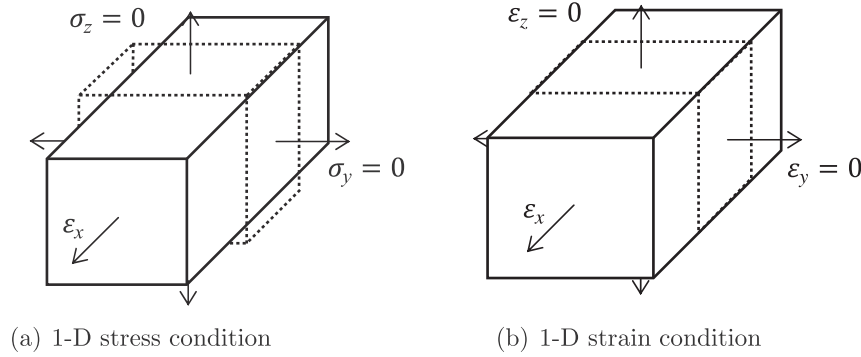
(a) 1-D stress condition   (b) 1-D strain condition

Fig. 1. Two constraint conditions.

stress. Thus, we employ here the virial definition without the kinetic portion [74] to calculate the macroscopic stress tensor of system:

$$\sigma_{\alpha\beta} = -\frac{1}{V}\left(\sum_i \sum_{j>i} r_{ij}^\alpha f_{ij}^\beta\right), \qquad (2)$$

where f_{ij} are interatomic forces of atom pairs $\langle ij \rangle$ with corresponding distance r_{ij}, α and β the Cartesian coordinates, V the voronoi volume of the specimen. Therefore, the hydrostatic stress σ_h of systems can be calculated by

$$\sigma_h = \frac{1}{3}\sum_\alpha \sigma_{\alpha\alpha} \qquad (3)$$

2.3. Critical strain rate

It is known that the dynamic response of metal differs from that of static state [75–78]. Since the parameters in MEAM potential are fitted by both results of ab-initio calculation under ground state and data from static experiments, it is necessary to evaluate the reliability of this potential under extremely high rate deformation. For a cubic box with edges length L of $32a_0$ and void radius r of $2a_0$, it was initially found that the differences between elastic constants calculated at various strain rates from 10^{11} s^{-1} to 10^8 s^{-1} are trivial; and all these data are close to the experimental results via ultrasonic pulse echo technique [79]. It seems that this MEAM

potential is reliable for elastic properties of vanadium even at strain rate as high as 10^{11} s^{-1}. However, the value of radial distribution function (RDF) at 1NN distance r_0 shows that there exists local disorder in system under high rate deformation:

$$g(r_0) = \frac{\sum_{i=1}^N g(n_i, r_0)}{N} = \frac{\sum_{i=1}^N \frac{n_i}{4\pi r_0^2 dr \bar\rho_n}}{N} \qquad (4)$$

where N is the total number of atoms, n_i the number of atoms in spherical shell centering at atom i with radius from $(r_0 - dr)$ to r_0, $\bar\rho_n$ the average number of atoms per unit volume under steady tension. In 1-D strain condition, $N = 65,477$, $dr = 0.00038$ Å, $\bar\rho_n = 0.07224$ Å^{-3} and $r_0 = 2.63879$ Å when $\varepsilon_x = 0.01$.

It can be seen from Fig. 2b that 10^9 s^{-1} is the critical strain rate above which $g(r_0)$ decreased with increasing strain rate indicating that there were fewer atoms at 1NN distance at higher rates. Since the total number of atom remained unchanged, this result implied that some atoms oscillated so heavily that they left the positions where they should be at steady state. The simulations by Braníco et al. [80] and Wright et al. [81] showed that the lattice is stable under low rate deformation, but becomes amorphous at higher rates. However, there would never exist a determinate *high* strain rate unless some criterion was set. For example, one would get a higher critical rate if a larger dr was used in Fig. 4. In the following studies, only $\dot\varepsilon_x \leqslant 10^9$ s^{-1} were applied, so as to eliminate the unnecessary oscillation of stress brought by local disorder; thus an identical stress–strain ratio at elastic stage can be kept in different strain rate cases.
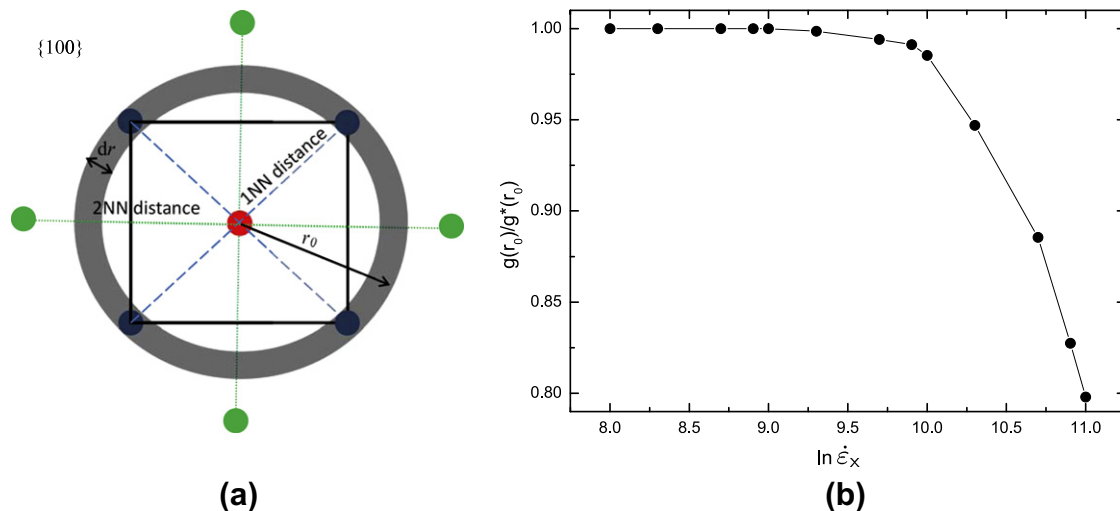

(a)   **(b)**

Fig. 2. (a). Illustration of radial distribution function (RDF) at the first nearest neighbor (1NN) distance r_0 on any {100} plane. (b). The normalized RDF at 1NN distance calculated at different strain rates. $g^*(r_0)$ is the value of $g(r_0)$ at $\dot\varepsilon_x = 10^8$ s^{-1}.

2.4. Highlight of dislocation and void surface

The configurations of atoms were colored using centrosymmetry parameter (CSP) [82], so as to highlight the dislocation and void surface. The idea of CSP comes from the fact that a centrosymmetric material (e.g., BCC lattice) will remain centrosymmetric under homogeneous elastic deformation, where each atom has pairs of equal and opposite bonds to its neighbors [83]. When a defect is introduced nearby, this equal and opposite relation no longer holds. Thus one can define the CSP which is zero for a centrosymmetric material under any homogeneous elastic deformation but non-zero for any plastic deformation. The original CSP for each atom i is defined as

$$c_i = \sum_{i=1}^{k} |\boldsymbol{R}_j + \boldsymbol{R}_{j+k}|^2 \tag{5}$$

where c_i is the CSP of atom i, $\boldsymbol{R}_j$ and $\boldsymbol{R}_{j+k}$ are the vectors of bonds corresponding to k pairs of opposite neighbors, see Fig. 3. The more distorted the local BCC lattice, the larger the CSP. An alternative CSP definition was proposed by Li [82] and implemented in the Atom-Eye visualization package; its definition follows

$$c_i = \frac{\sum_{l=1}^{k/2} D_l}{2\sum_{j=1}^{k} |\boldsymbol{R}_j|^2}, \tag{6}$$

where the function $D_l = |\boldsymbol{R}_l + \boldsymbol{R}_{l'}|^2$ is minimized by bond $\boldsymbol{R}_{l'}$. c_i is dimensionless with a maximum value of 1. This implementation has the advantage of finding dynamically the best opposite pairs of atoms as it is required for a real time analysis of an arbitrary structure being visualized [84]. Seven pairs within 2NN shell in perfect BCC lattice are summed over, which has been proved to be less noisy than summing over the four pairs within 1NN shell [20]. In our snapshots, only atoms with $c_i \geqslant 0.01$ were visible (see Fig. 4).

2.5. MSD of void surface atoms

Mean square displacement (MSD) is usually used for measuring the average distances some given atoms travel, showing how often the atoms suffer collisions in liquid or gas:

$$M = \left\langle \left| \sum_{i=1}^{h} \boldsymbol{R}_i - \boldsymbol{R}_c \right|^2 \right\rangle \tag{7}$$

where M is the MSD of specified atoms, $\boldsymbol{R}_i$ the displacement vector of atom i, $\boldsymbol{R}_c$ the displacement vector of center of mass of these

Fig. 4. Illustration of mean square displacement (MSD) of void surface atoms. $\boldsymbol{R}_i$ and $\boldsymbol{R}_c$ correspond to the displacement vectors of atom i and the center of mass of surface atoms, respectively.

atoms, and h the number of specified atoms. The square is then averaged among time. If the system has been well relaxed and is not being deformed, the MSD of void surface atoms, which are determined by their CSP, remains unchanged during MD running. However, as void grows, the MSD of surface atoms increases, and it can geometrically depict the void evolution. The authors [9] have used MSD to study cylindrical voids growth in 2-D specimen, and will extent this method to the spherical void in 3-D specimen here.

3. Results and discussion

3.1. Strain rate dependence

Seven different strain rates, from 10^9 s^{-1} to $5 \times 10^7 \text{ s}^{-1}$, were applied independently on box established in Section 2.3 under two constraint conditions. Specimen of the same size but with no void was also elongated at the same rates under 1-D stress condition. Snapshots of atoms colored by CSP are shown in Fig. 5, where $\langle 1\,1\,1\rangle\{1\,1\,0\}$ dislocations were punched out from the void surface. This process is schematically shown in Fig. 6. The shear loops were initially emitted at point A, where the shear stress is maximal under 1-D tension along x axis. The edge components of loop moved so fast at 10 K that the segments became straight. When loops expanded to point B and C, where $[\bar{1}\,1\,1]$ and $[1\,1\,1]$ directions intersected the void surface respectively, the dislocation had no edge components, and the remaining purely screw cores split on three non-planar $\{1\,1\,0\}$ planes. At point C, for instance, there is:

$$\frac{a}{2}[1\,1\,1](0\,1\,\bar{1}) \Rightarrow \frac{a}{4}[1\,1\,1](0\,1\,\bar{1}) + \frac{a}{8}[0\,1\,1](0\,1\,\bar{1}) + \frac{a}{8}[1\,0\,1]$$
$$\times (1\,0\,\bar{1}) + \frac{a}{8}[1\,1\,0](1\,\bar{1}\,0) \tag{8}$$

Then the shear stress on void surface σ_s compressed the $[0\,1\,1](0\,1\,\bar{1})$ factional dislocation inward, leaving a more stable two-fold non-planar screw core with $[1\,1\,0](1\,\bar{1}\,0)$ and $[1\,0\,1]$ $(1\,0\,\bar{1})$ fractional dislocations, which stuck at point C. Thus, the screw dislocations at point B and C became a Frank-Read dislocation source, and $[\bar{1}\,1\,1](0\,1\,\bar{1})$ and $[1\,1\,1]\,(0\,1\,\bar{1})$ perfect dislocations continued slipping outward so that a shear loop was formed. The extremities of these loops had to remain connected to the void
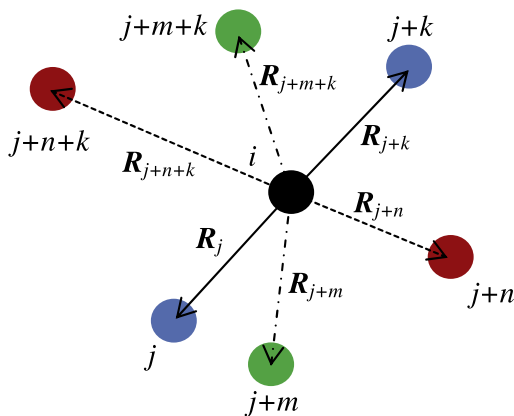

Fig. 3. Atom i with a non-zero centrosymmetry parameter (CSP) due to its three pairs of neighbors, k is the number of its neighbors. The bonds pair formed by $\langle \boldsymbol{R}_j, \boldsymbol{R}_{j+k} \rangle$ is equal and opposite, while that by $\langle \boldsymbol{R}_{j+m}, \boldsymbol{R}_{j+m+k} \rangle$ is equal but not opposite, and that by $\langle \boldsymbol{R}_{j+n}, \boldsymbol{R}_{j+n+k} \rangle$ is opposite but not equal. Both sums of vectors of the last two bond pairs are non-zero.
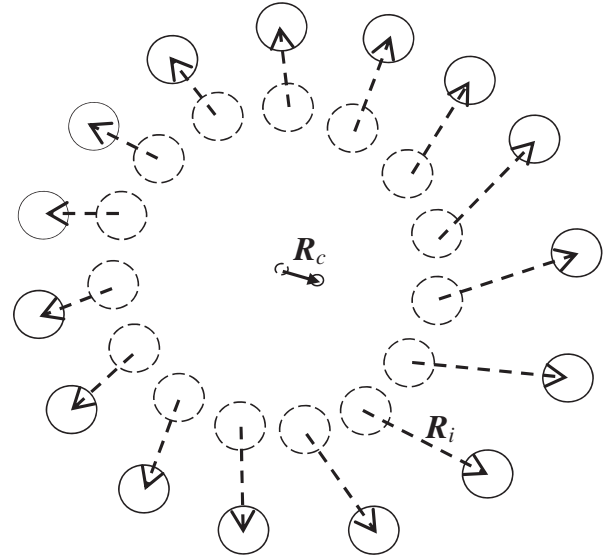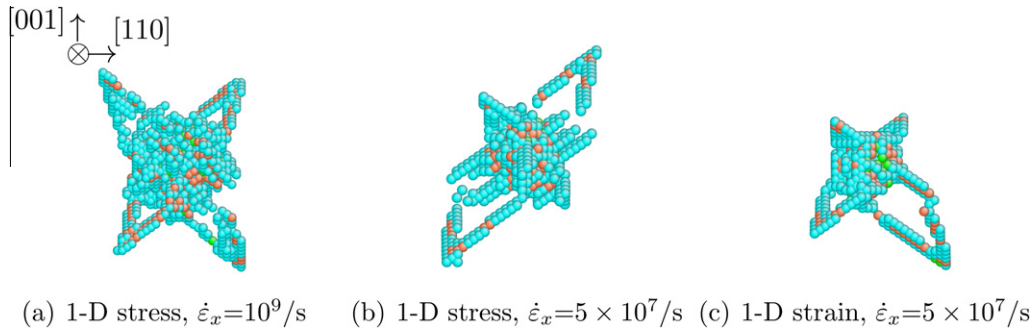
(a) 1-D stress, $\dot{\varepsilon}_x = 10^9/s$ (b) 1-D stress, $\dot{\varepsilon}_x = 5 \times 10^7/s$ (c) 1-D strain, $\dot{\varepsilon}_x = 5 \times 10^7/s$

Fig. 5. Snapshots from MD simulations for $[\bar{1}10]$ direction at peak stress point of each case. $\langle 111 \rangle \{110\}$ shear loops were observed emitted from the void surface. Dislocation asymmetry is more noticeable in low rate and small triaxiality cases.
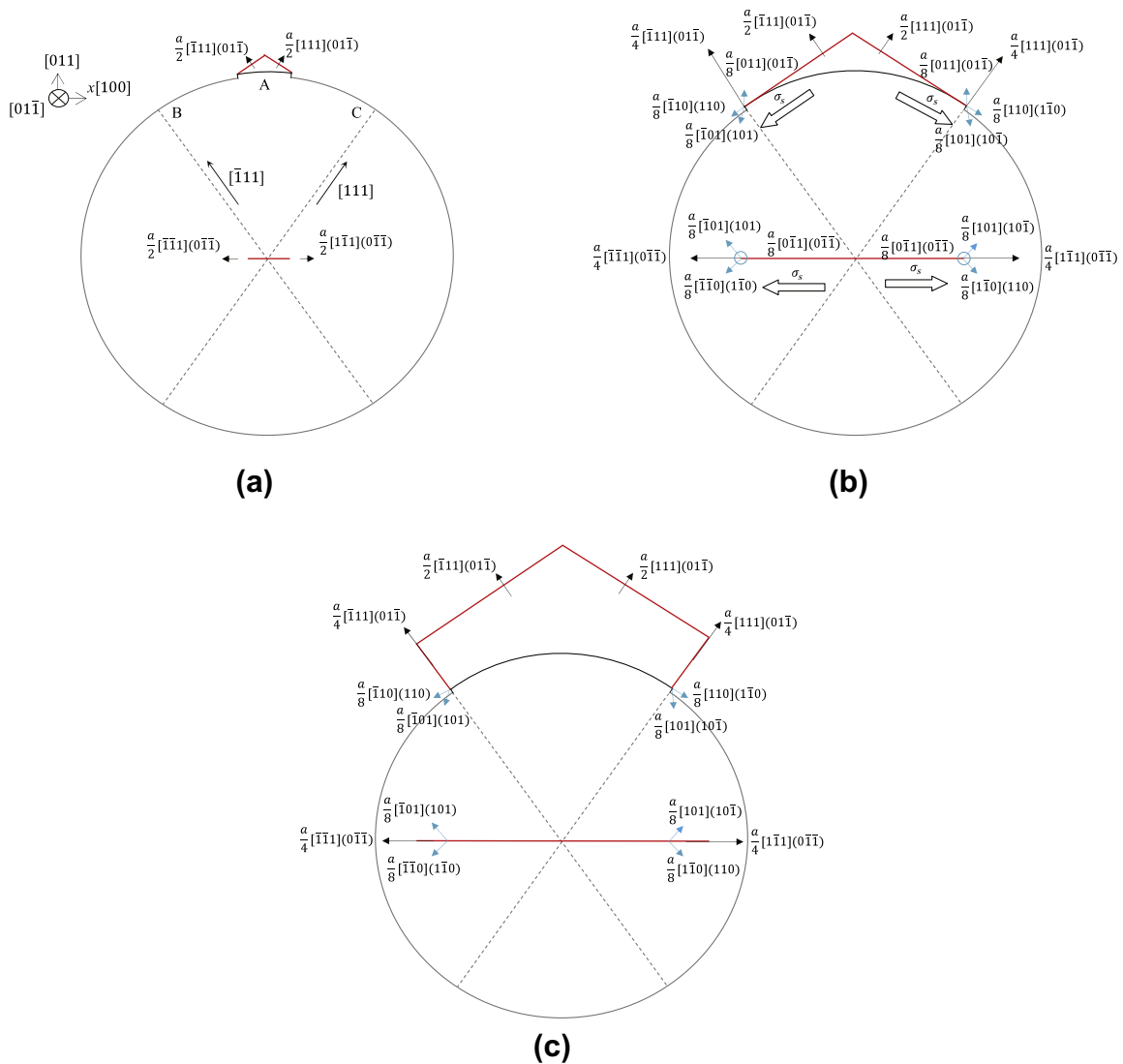

Fig. 6. Schematic showing of emission of $\langle 111 \rangle \{110\}$ shear loops (red lines). (a) Initial emission of dislocations from point A, where the shear stress is maximal under 1-D tension along x axis. The $[111]$ and $[\bar{1}11]$ directions intersected the void surface at points B and C, respectively. (b) At point C, the dislocation had no edge components, and the remaining screw cores split on three non-planar $\{110\}$ planes (blue arrows). Then the shear stress on void surface σ_s compressed the $[011](01\bar{1})$ factional dislocation inward, leaving a more stable two-fold non-planar screw core with $[110](1\bar{1}0)$ and $[101](10\bar{1})$ dislocations, which stuck at point C. (c) $[\bar{1}11](01\bar{1})$ and $[111](01\bar{1})$ perfect dislocations continued slipping outward so that a shear loop was formed.

so as to expand the void volume, as has been well discussed by Bulatov et al. [85] and Bringa et al. [86]. Tang et al. [46] investigated the growth of nanoscale voids for BCC Ta under uniaxial ten-

sile strain, and observed the nucleations of $\{112\}$ shear loops at 300 K by adjacent $\{110\}$ stacking faults intersecting the void surface at 45°, which were absent in our simulations. This difference

may be contributed to the much lower temperature of 10 K employed here.

Noticeable asymmetry of loops is also observed from the snapshots: under the same constraint condition, the loops were more symmetric at higher rate; while at the same rate, symmetry was more likely to appear in 1-D strain case, where the triaxiality was larger. Rudd [20] considered this asymmetry as the result of randomness of rare events, such as nucleation of dislocations on thermally preferable glide systems among all cubically equivalent ones. This explanation is also valid here: the higher stress accompanied with either higher strain rate or larger triaxiality led to stronger atomic vibrations, which reduced the fluctuations brought by heterogenous thermal activations.

It is found from Fig. 7 that the hydrostatic stress in specimen under 1-D strain tension is the highest, where the triaxiality of box is the largest. In the other two cases, the stress–strain ratio are identical at the elastic stage, which means that the void is too small to influence the modulus of material. Additionally, in each case, the higher the strain rate, the larger the peak stress. This is because a higher macro strain rate led to a higher shear strain rate on void surface, where the dislocation velocity was higher; this higher velocity needed to be driven by a larger shear stress, which in our study, came from nowhere else but a larger macro stress.

It is also found that the stress of intact specimen dropped sharply at yield point. This is attributed to the homogeneous dislocations all through the box, as found by Tschopp et al. [87]. These instantly nucleated dislocations led to an unstable lattice, accounting for the stress oscillations at point B in Fig. 7a. Because of the more uniform thermal activations under larger stress as mentioned above, the oscillations were smaller for higher rate cases. As for void contained specimen, especially at higher rate, however, the dislocations were nucleated at void surface when stress–strain curve deviated from straight line, then the stress continued increasing till the peak stress point. Thus, we identified the yield point as the point when linearity between stress and strain broke down. By this definition, the relationship between hydrostatic yield stress σ_Y and σ_x at yield point in 1-D strain condition is found to agree well with the model by Kanel et al. [88]:

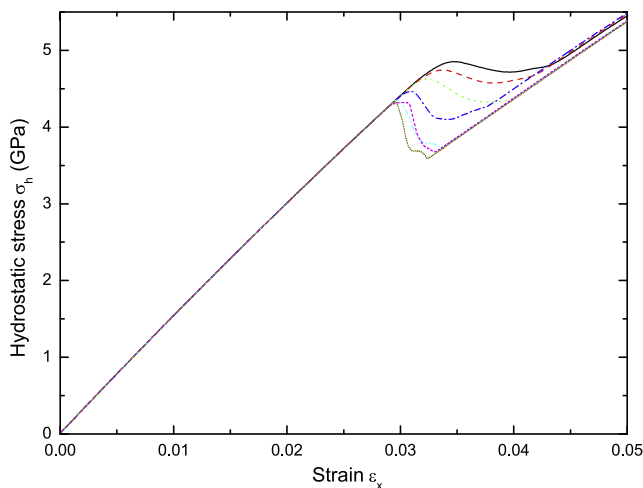$$\sigma_Y = \frac{1}{3}\left(1 + 2\frac{C_{12}}{C_{11}}\right)\sigma_x \tag{9}$$

where elastic constants of vanadium $C_{11} = 232.4$ GPa, $C_{12} = 119.36$ GPa. According to Rudd [20], time is needed in high rate case for release wave to propagate through the box; in low rate case, once the void surface is yielded, the void grows faster than box vol-
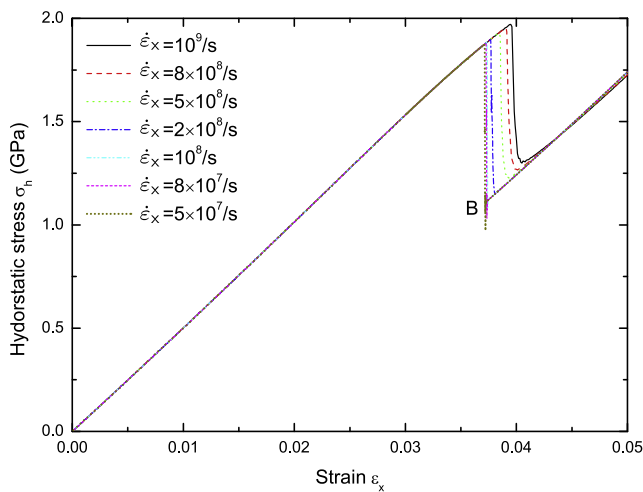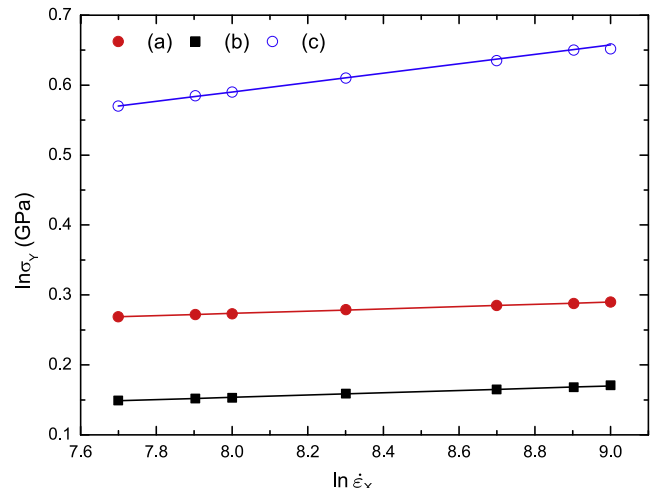

(a) Intact box, 1-D stress condition
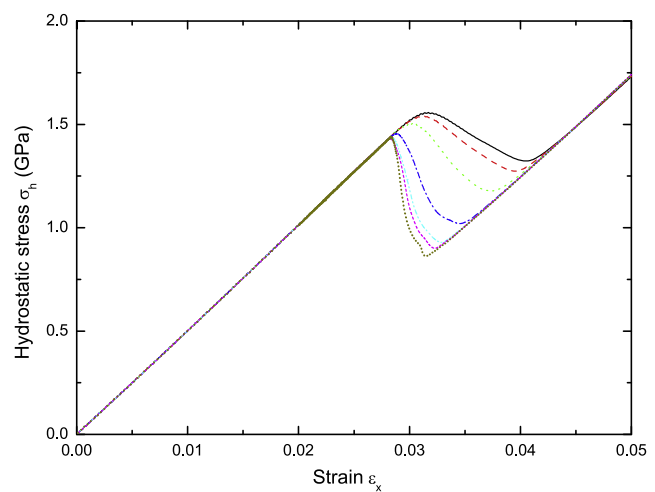
(b) Void contained box, 1-D stress condition

(c) Void contained box, 1-D strain condition

(d) Hydrostatic yield stress in each case

Fig. 7. (a–c). Stress–strain response of void contained box and intact box, under different constraint conditions; (d). Hydrostatic yield stresses in three cases. Note that σ_h in (a) went through oscillation at point B in lower rate cases.

ume, and so this inertial effect is trivial. The relationship between void(box) growth rate and stress change around peak point at different strain rates were also reported in other work [2]. In continuum solid mechanics, the porosity f and the hydrostatic plastic strain ε_h^p are related by [89]

$$\frac{\dot{f}}{3(1-f)} = \dot{\varepsilon}_h^p \tag{10}$$

where the dots denote time derivatives. This equation agrees well with MD simulations as long as f is small [2]. $\dot{\varepsilon}_h^p$ can be written as

$$\dot{\varepsilon}_h^p = \frac{1}{3}\sum_\alpha \dot{\varepsilon}_{\alpha\alpha}^p = \frac{1}{3}\sum_\alpha (\dot{\varepsilon}_{\alpha\alpha} - S\dot{\sigma}_{\alpha\alpha}) = \dot{\varepsilon}_h - S\dot{\sigma}_h \tag{11}$$

where S is the elastic compliance tensor, $\dot{\varepsilon}_h$ the hydrostatic strain rate. At elastic stage, $\dot{\varepsilon}_h$ equals $S\dot{\sigma}_h$; then from yield point to peak point, $\dot{\sigma}_h$ decreases to 0, when

$$\frac{\dot{f}}{3(1-f)} = \dot{\varepsilon}_h \tag{12}$$

Since void fraction is small even at peak point, f can be considered as a constant in our discussion. When $\dot{\varepsilon}_x = 5 \times 10^7\ s^{-1}$, Eq. 12 is valid at yield point, which, therefore, is also the peak point. From [22,23,30,90,91], one gets

$$\dot{V}_{void} \sim v_{loop} \sim \sigma_Y \sim (\dot{\varepsilon}_x)^m \tag{13}$$

where V_{void} is the void volume, v_{loop} the dislocation loop velocity, m the strain rate sensitivity. We also have

$$f = \frac{V_{void}}{V} \Rightarrow \dot{V}_{void} = \dot{f}V + fV_0\dot{\varepsilon}_x \tag{14}$$

where V_0 is the initial box volume. So we get

$$\dot{f} \sim \frac{1}{V}\left[(\dot{\varepsilon}_x)^m - fV_0\dot{\varepsilon}_x\right] \tag{15}$$

Note that $\dot{\varepsilon}_h$ varies linearly with respect to $\dot{\varepsilon}_x$ no matter what the loading pattern is. In our simulations, m is 0.067 for 1-D strain and 0.016 for 1-D stress condition, see Fig. 7d. Like the modulus, m is not affected by the existence of void, but by the constraint condition. Since $m < 1$, porosity growth rate $\dot{f}$ increases slower than strain rate as the later one increases. Thus, there exists a strain rate at which Eq. 12 is satisfied precisely once the surface is yielded, so the yield point and peak point coincide; with rate increasing,

though $\dot{f}$ at yield point is higher than that in lower rate case, it needs some time to grow to catch up with $3(1-f)\dot{\varepsilon}_h$, only then does the hydrostatic stress start to drop.

In 1-D stress condition where Poisson effect is allowed, some similar phenomenons are found, see Fig. 8. For intact specimen, the shrinkage of transverse edges decreased abruptly at yield point; while for void contained box, the dropping was rounded. In the later case, oscillations of Poisson ratio are observed, which were larger at lower strain rate; also, the transverse edges length change around the yield point was less violent at higher rate. The later situation can be explained by both the inadequate void growth rate at high rate as stated above, and the traditional estimation of the size of plastic zone around the void by Hill [92]:

$$r_{zone} = \left(\frac{2E}{3\sigma_Y}\right)^{\frac{1}{3}} r \tag{16}$$

where the Young's modulus $E = 151.4$ GPa. For void contained box, σ_Y was lower at lower strain rate, leading to a larger plastic zone, making the material surrounding the void stronger, so Poisson effect was less noticeable.

The MSD of void surface atoms calculated by Eq. 7 are shown in Fig. 9. It is seen that MSD dropped at yield point at lower strain rate in both constraint conditions, meaning that some surface atoms turned inward. Through more detailed examinations, where all surface atoms were divided into several groups, it is shown that the dropping of MSD was attributed to the asymmetric dislocation loops, which transferred the adjacent atoms away from the void, thus driving atoms at the opposite surface, where much fewer dislocations were nucleated, towards their original positions.

3.2. Initial porosity effects

Two series of simulations were performed at strain rate of $10^9\ s^{-1}$ under 1-D stress condition. The specimens in the first series have a fixed edge length L of $32a_0$, with initial void radius r varying from $0.5a_0$ to $10a_0$; in the other series, when initial void radius remains $4a_0$, boxes with different edge length from $16a_0$ to $64a_0$ were deformed.

For the first series, it is noteworthy that when $r = 0.5a_0$, only one atom was cut from the box, i.e., vacancy contained box, yet its yield stress is significantly lower than that of intact box, and higher than that of box with void of $r = a_0$, where 15 atoms were deleted. For
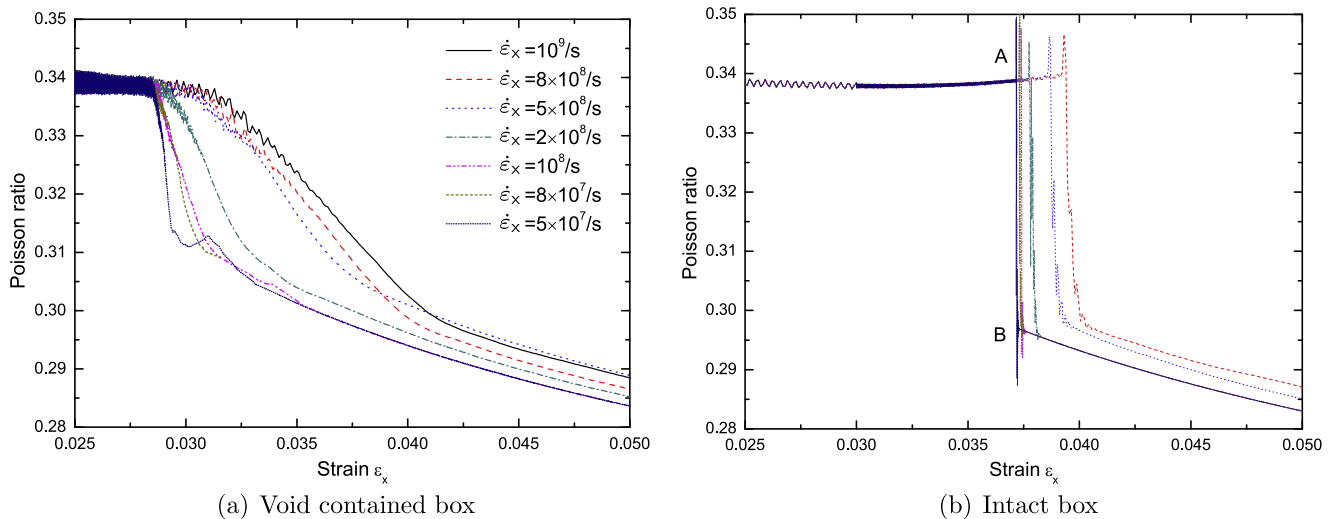

(a) Void contained box

(b) Intact box

Fig. 8. Poisson ratio of the void contained box and intact box, under 1-D stress condition. In (b), oscillations of poisson ratio were observed at lower strain rates, see points A and B.
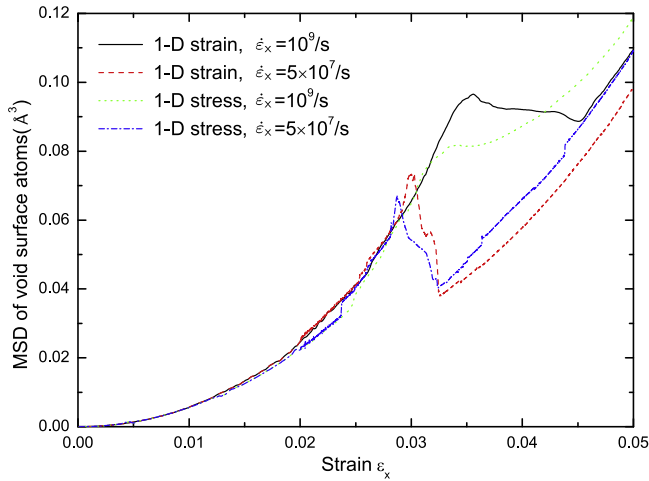
Fig. 9. Mean square displacement of void surface atoms at rates of $10^9 \, s^{-1}$ and $5 \times 10^7 \, s^{-1}$ under both constraint conditions. Note that MSD decreased at yield point when strain rate was low.

vacancy contained box, the plasticity mechanism was different from void contained one that some dislocations (marked by dash arrow in Fig. 10a) were nucleated independently of the vacancy. Nanovoid growth simulations in single crystalline Cu by Bringa et al. [30] showed that the loops are nucleated homogeneously in box missing one atom; for box containing two or four vacancies, loops attached to vacancies surface form sequentially as defect grows. In this study, we consider the defect, where all dislocations were nucleated at its surface, as a void. Yet it is unclear that how many adjacent vacancies are sufficient to form a void in other materials.

It is known that the coalescence between a single void with its periodic images and that between an isolated pair of voids are markedly different [19]. As initial void radius increased, dislocations were nucleated on all {110} planes, see Fig. 10b, where the void diameter was equal to the intervoid ligament distance (ILD) [19] between void and its periodic images. With even larger initial void, ILD was smaller than void diameter, thus the interaction between neighboring images was more prominent. It is seen from Fig. 10c that there were eight isolated dislocations (one of them is marked by dash arrow) apart from those at void surface. These unattached dislocations were nucleated from perfect lattice due to the concentrated shear stress between periodic images.

It is also found that both the yield stress and Young's modulus decreased along with larger porosity, see Fig. 11. In addition, the larger the porosity, the larger the Poisson ratio and the smaller the MSD of surface atoms at elastic stage in both series. This

relationship between porosity and void growth rate indicated by MSD was also reported in simulations of single void growth in Cu by Seppälä et al. [19] that the normalized void volume grows slower when porosity is larger. This agreement implied the ability of MSD to reflect the void volume evolution. Furthermore, it is shown that even under the same porosity, the Young's modulus of small box is smaller than that of large box, and this phenomenon is specimen size effect, as will be discussed below.

3.3. Specimen size effects

Simulations where L/r was fixed as 16 were performed at rate of $10^9 \, s^{-1}$ under 1-D stress condition. L varies from $16a_0$ to $128a_0$. It is of interest that, in our largest void case where $r = 24.29 \, \text{Å}$, unlike the shear loops emitted from the surface of small void, triangular prismatic loops were nucleated on (011) and $(0\bar{1}1)$ planes, see dash arrows in Fig. 12a. The loops here concurred with the simulations by Rudd [20], where prismatic loops were punched out from surface of void with radius of 18.88 Å in BCC Mo and 33.06 Å in BCC Ta. Tang et al. [46] observed for void evolution in BCC Ta under hydrostatic tension that the screw components of three shear loops with the same Burgers vector but opposite dislocation line directions annihilate, and the remaining edge components are connected with each other to form a triangular prismatic loop. This mechanism may not be valid here since the void contained box was not under 3-D tension. The simulations of Bringa et al. [30] showed that, when void size rises, the sphericity of void increases, and the ledges on void surface may influence the dislocation nucleation. In our deformations at 10 K, when the void was small, the attached shear loops emitted from void surface were the main mechanism of plasticity; but when initial void size increased, the adjacent shear loops would intersect each other in some way to form the prismatic loops on {110} planes. We believe that the ledges along the void surface also have a significant effect on the generations of prismatic dislocations, yet the detailed process remains an open question for further study.

It is also found that the hydrostatic yield stress σ_Y in constant porosity series, constant box edge length series and constant void radius series decreased as the initial void radius and porosity grew. The data are plotted in Fig. 13b and compared with the continuum analysis of Lubarda et al. [22]:

$$\frac{\sigma_{cr}}{G} = \frac{b/r}{\sqrt{2}\pi(1-v)} \frac{(1+\sqrt{2}w/r)^4 + 1}{(1+\sqrt{2}w/r)^4 - 1}$$

(17)

where σ_{cr} is the critical stress at void surface required for dislocation emission, G the shear modulus, v the Poisson ratio of material, b the magnitude of Burgers vector of dislocation, and w the dislocation width. Under 1-D stress condition, $\sigma_{cr} = 6\sigma_Y$, $G = 45.95 \, \text{GPa}$, $v = 0.34$ and $b = \sqrt{3}a_0/2$. This equation is quite general by firstly considering an edge dislocation near a void, then its equilibrium
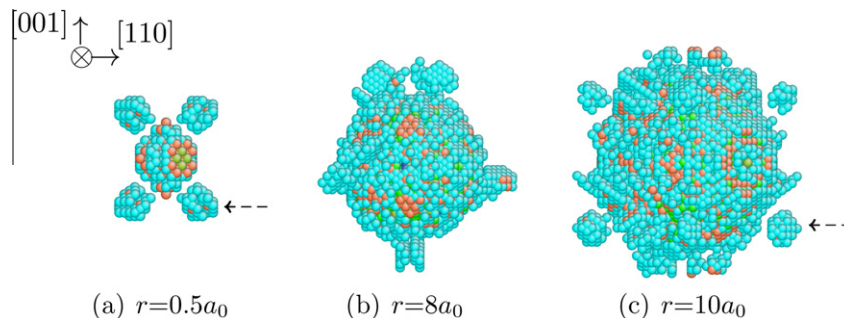

Fig. 10. Snapshots from MD simulations for $[\bar{1}10]$ direction at peak stress point of each case when $L = 32a_0$. In (a) and (c), some dislocations were nucleated independently of the initial defect (dash arrows). In (b), dislocations were nucleated on all {110} planes.
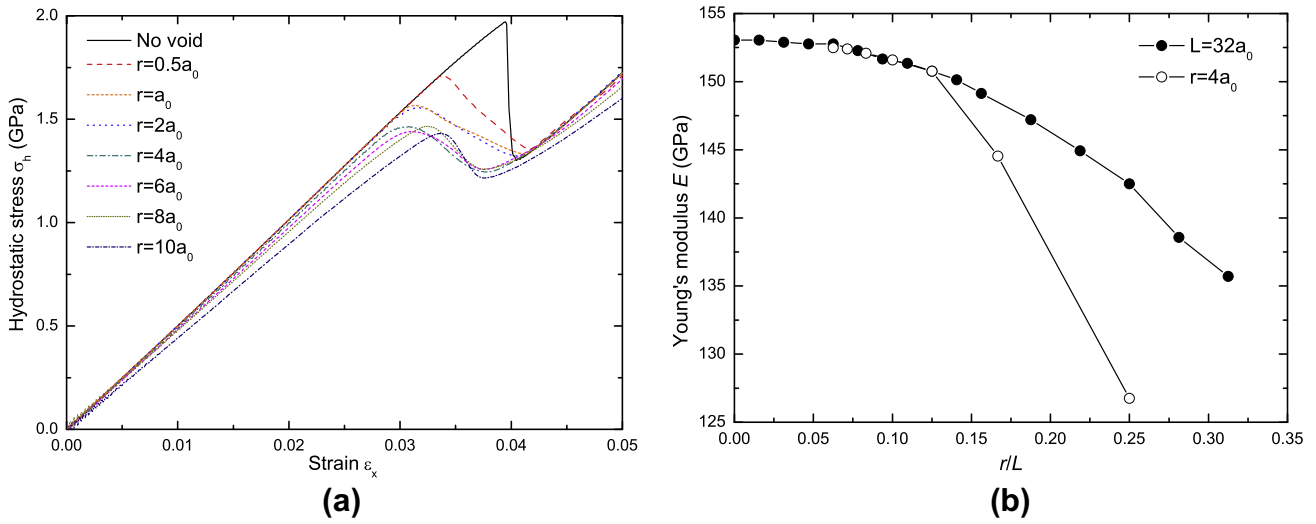
Fig. 11. (a) Stress–strain response of specimen with box edge length $L = 32a_0$, the void radius varies from $0.5a_0$ to $10a_0$. (b) Young's modulus of specimen in both constant box edge length and constant void radius series. The results from intact box are also shown.
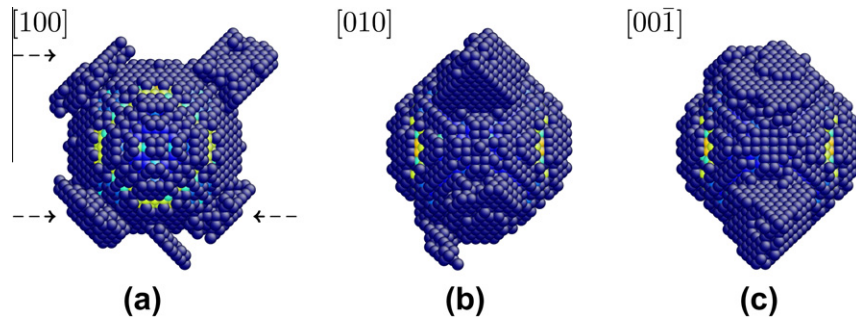

Fig. 12. Snapshots from MD simulations for $\langle 1\,0\,0 \rangle$ directions at peak stress point. The box edge length is $128a_0$, with void radius of $8a_0$. Triangular prismatic loops (dash arrows) were formed on $(0\,1\,1)$ and $(0\,\bar{1}\,1)$ planes.
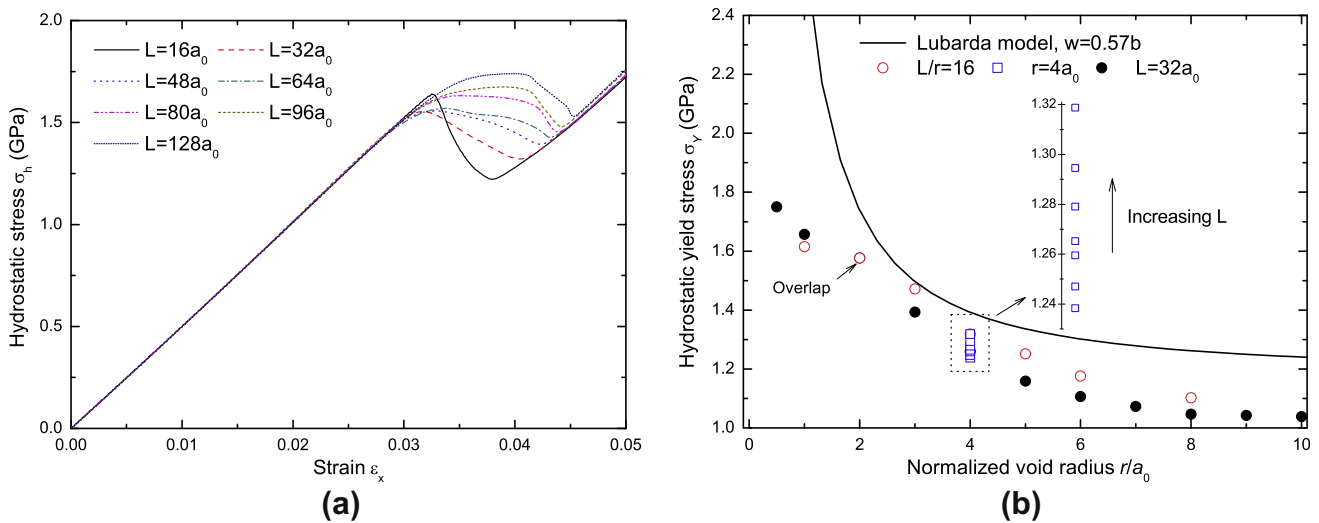

Fig. 13. (a) Stress–strain response of specimen with $L/r = 16$. (b) Hydrostatic yield stress as a function of normalized void radius from our MD simulations and prediction of Lubarda et al. [22].

position from the void surface d_{cr}, where the attraction from the void is balanced by the local stress, is given out by classical elastic field theory, where r is supposed to be larger than $3w$ [22]. Then if $d_{cr} = w$, the dislocation is likely be emitted from the void surface. In

our simulations, the initial shear loops formed at point A in Fig. 6a contained mainly the edge components, and the dislocation width w equals $0.57b$ for BCC vanadium [93]. Therefore, it is reasonable that σ_Y calculated here is in well agreement with the results by

Lubarda equation when $w = 0.57b$. When r went to zero, Lubarda equation failed, as expected.

4. Conclusions

1. There exists a critical strain rate above which vanadium MEAM potential is not suitable. The RDF of system at 1NN distance showed that the amplitude of oscillations of atoms were larger in higher rate case, making the local lattice unstable.

2. When void radius was eight times of the lattice constant and the porosity was not very large, triangular prismatic loops were observed at void surface on {1 1 0} planes. When void radius was twice the lattice constant with the same porosity, $\langle 1 1 1 \rangle\{1 1 0\}$ dislocations with straight segments were punched out from void surface, then after some time the screw components of the dislocations split on three non-planar planes and became two-fold non-planar screw cores under compression. The two-fold cores played a role as Frank–Read dislocation source, and thus the shear loops were formed. The asymmetry of loops was more noticeable in cases with lower rate and smaller triaxiality.

3. The yield point was identified as the breakdown of the linearity between stress and strain, and was the highest in fully constraint condition with the largest triaxiality. For intact box, the stress dropped sharply at yield point with noticeable oscillations; for void contained box, the yield point and peak stress point coincided at low strain rate, yet the two points separated as rate increased due to the inadequate void growth rate. Similar phenomenons were observed for Poisson ratio. Moreover, the yield stress decreased along with increasing initial void radius and porosity. The hydrostatic yield stress calculated by our MD simulations agreed well with that from Lubarda equation, especially for large void.

4. MSD of surface atoms was applicable for geometrically depicting the void evolution. It dropped at yield point in low rate case due to the asymmetric dislocation loops.

5. Homogenous nucleations involved in the plasticity mechanism of vacancy contained box. As initial void radius increased, dislocations were nucleated on all {1 1 0} planes. When porosity was so large that the void diameter surpassed the ligament distance between void and its periodic images, the interactions between periodically neighboring voids were noticeable, leading to isolated dislocations unattached to void at yield point. In addition, as initial porosity rose, Young's modulus and the MSD of surface atoms dropped while the Poisson ratio increased.

Acknowledgments

References

[1] S.N. Nasser, M. Hori, J. Appl. Phys. 62 (1987) 2746.
[2] E.T. Seppälä, J. Belak, R.E. Rudd, Phys. Rev. B 69 (2004) 134101.
[3] M. Hori, S.N. Nasser, Mech. Mater. 7 (1988) 1.
[4] P.E. Magnusen, D.J. Srolovitz, D.A. Koss, Acta Metall. Mater. 38 (1990) 1013.
[5] X.X. Zhang, Z.S. Cui, Appl. Math. Mech. – Engl. Ed. 30 (2009) 631.
[6] M. Pelfort, Y.N. Osetsky, A. Serra, Philos. Mag. A 81 (2001) 803.
[7] S.T. Revankar, T. Croy, Exp. Therm. Fluid Sci. 31 (2007) 181.
[8] Y.N. Osersky, D.J. Bacon, J. Nucl. Mater. 323 (2003) 268.
[9] S.Z. Xu, Z.M. Hao, Q. Wan, IOP Conf. Ser.: Mater. Sci. Eng. 10 (2010) 012175.
[10] J.P. Feng, F.Q. Jing, G.R. Zhang, J. Appl. Phys. 81 (1997) 2575.
[11] Y.L. Bai, Z. Ling, L.M. Luo, F.J. Ke, J. Appl. Phys. 89 (1992) 622.
[12] X.S. Xing, Eng. Fract. Mech. 37 (1990) 1099.
[13] F.D. Fischer, J. Svoboda, Scripta Mater. 58 (2008) 93.
[14] A.M. Cuitiño, M. Ortiz, Acta Mater. 44 (1996) 427.
[15] J. Belak, in: Proc. 1997 APS Topical Conf. on Shock Compression of Condens. Matter, 1997, pp. 211.
[16] J. Belak, J. Comput. Aied. Mater. Des. 5 (1998) 193.
[17] R.E. Rudd, J.F. Belak, Comput. Mater. Sci. 24 (2002) 148.
[18] R.E. Rudd, E.T. Seppälä, L.M. Dupuy, J. Belak, J. Comput. Aid. Mater. Des. 14 (2007) 425.
[19] E.T. Seppälä, J. Belak, R.E. Rudd, Phys. Rev. B 71 (2005) 064112.
[20] R.E. Rudd, Philos. Mag. 89 (2009) 3133.
[21] A.L. Stevens, L. Davison, W.E. Warren, J. Appl. Phys. 43 (1972) 12.
[22] V.A. Lubarda, M.S. Schneider, D.H. Kalantar, B.A. Remington, M.A. Meyers, Acta Mater. 52 (2004) 1397.
[23] S. Traiviratana, E.M. Bringa, D.J. Benson, M.A. Meyers, Acta Mater. 56 (2008) 3874.
[24] J. Marian, J. Knap, M. Ortiz, Phys. Rev. Lett. 93 (2004) 165503.
[25] V.A. Lubarda, Int. J. Plast. 27 (2010) 181.
[26] K.J. Zhao, L.L. Fan, C.Q. Chen, Acta Mech. Solida Sinica 22 (2009) 650.
[27] D.C. Ahn, P. Sofronis, M. Kumar, J. Belak, R. Minich, J. Appl. Phys. 101 (2007) 063514.
[28] L. Farrissey, M. Ludwig, P.E. McHugh, S. Schmauder, Comput. Mater. Sci. 18 (2000) 102.
[29] K.J. Zhao, C.Q. Chen, Y.P. Shen, T.J. Lu, Comput. Mater. Sci. 46 (2009) 749.
[30] E.M. Bringa, S. Traiviratana, M.A. Meyers, Acta Mater. 58 (2010) 4458.
[31] W.J. Jun, Z.F. Song, X.L. Deng, H.L. He, X.Y. Cheng, Phys. Rev. B 75 (2007) 024104.
[32] T. Hatano, Phys. Rev. Lett. 93 (2004) 085501.
[33] L.P. Davila, P. Erhart, E.M. Bringa, M.A. Meyers, V.A. Lubarda, M.S. Schneider, R. Becker, M. Kumar, Appl. Phys. Lett. 86 (2005) 161902.
[34] G.P. Potirniche, M.F. Horstemeyer, G.J. Wagner, P.M. Gullett, Int. J. Plast. 22 (2006) 257.
[35] T. Hatano, H. Matsui, Phys. Rev. B 72 (2005) 094105.
[36] D. Terentyev, D.J. Bacon, Y.N. Osetsky, J. Phys: Condens. Matter 20 (2008) 445007.
[37] H.J. Lee, B.D. Wirth, J. Nucl. Mater. 386 (2009) 115.
[38] D. Stewart, K.S. Cheong, Curr. Appl. Phys. 8 (2008) 494.
[39] Y. Cheng, E. Bitzek, D. Weygand, P. Gumbsch, Modell. Simul. Mater. Sci. Eng. 18 (2010) 025006.
[40] V.I. Dubinko, N.P. Lazarev, Nucl. Instrum. Methods Phys. Res., Sect. B 228 (2005) 187.
[41] N.P. Lazarev, V.I. Dubinko, Radiat. Eff. Defects Solids 158 (2003) 803.
[42] Y.N. Osetsky, D.J. Bacon, Mater. Sci. Eng. A 400 (2005) 374.
[43] R. Gröger, V. Vitek, Mater. Sci. Forum 482 (2005) 123.
[44] K. Ito, V. Vitek, Philos. Mag. A 81 (2001) 1387.
[45] J. Marian, J. Knap, G.H. Campbell, Acta Mater. 56 (2008) 2389.
[46] Y.Z. Tang, E.M. Bringa, B.A. Remington, M.A. Meyers, Acta Mater. 59 (2011) 1354.
[47] M. Satou, S. Yip, K. Abe, J. Nucl. Mater. 307 (2002) 1007.
[48] K. Morishita, T. Diaz de la Rubia, E. Alonso, N. Sekimura, N. Yoshida, J. Nucl. Mater. 283 (2000) 753.
[49] K. Morishita, T. Diaz de la Rubia, J. Nucl. Mater. 271 (1999) 35.
[50] K. Morishita, N. Sekimura, T. Diaz de la Rubia, J. Nucl. Mater. 248 (1997) 400.
[51] J. Chen, L. Lu, K. Lu, Scripta Mater. 54 (2006) 1913.
[52] R. Schwaiger, B. Moser, M. Dao, N. Chollacoop, S. Suresh, Acta Mater. 51 (2003) 5159.
[53] Y.M. Wang, E. Ma, Appl. Phys. Lett. 83 (2003) 3165.
[54] M.T. McDowell, A.M. Leach, K. Gall, Modell. Simul. Mater. Sci. Eng. 16 (2008) 045003.
[55] M.F. Horstemeyer, M.I. Baskes, S.J. Plimpton, Acta Mater. 49 (2001) 4363.
[56] S.Y. Hu, M. Ludwig, P. Kizler, S. Schmauder, Modell. Simul. Mater. Sci. Eng. 6 (1998) 567.
[57] T. Kitamura, K. Yashiro, R. Ohtani, JSME Int. J. Ser. A, Mech. Mater. Eng. 40 (1997) 430.
[58] M.S. Daw, M.I. Baskes, Phys. Rev. B 29 (1984) 6443.
[59] M.I. Baskes, Phys. Rev. B 46 (1992) 2727.
[60] S.G. Kim, M.F. Horstemeyer, M.I. Baskes, M.R. Rohani, et al., J. Eng. Mater. Technol. 131 (2009) 041210.
[61] S.J. Plimpton, J. Comput. Phys. 117 (1995) 1.
[62] W.G. Hoover, Phys. Rev. A 31 (1985) 1695.
[63] W.G. Hoover, Phys. Rev. A 34 (1986) 2499.
[64] P.A. Gordon, T. Neeraj, Y. Li, J. Li, Modell. Simul. Mater. Sci. Eng. 18 (2010) 085008.
[65] A.H.W. Ngan, H.F. Zhang, Mater. Res. Soc. Symp. Process. 539 (1999) 69.
[66] C.R. Weinberger, W. Cai, Proc. Natl. Acad. Sci. USA 105 (2008) 14304.
[67] S.V. Bobylev, T. Ishizaki, S. Kuramoto, I.A. Ovid'ko, Phys. Rev. B 77 (2008) 094115.
[68] V. Vitek, M. Mrovec, J.L. Bassani, Mater. Sci. Eng. A 365 (2004) 31.
[69] F. Louchet, J. Phys. IV 3 (1993) 567.
[70] M. Parrinello, A. Rahman, J. Appl. Phys. 52 (1981) 7182.
[71] R. Clausius, Philos. Mag. 40 (1870) 122.
[72] M. Born, K. Huang, Dynamical Theory of Crystal Lattices, Clarendon Press, Oxford, 1988.
[73] M. Zhou, D. McDowell, Philos. Mag. A 82 (2002) 2547.
[74] M. Zhou, Proc. R. Soc. Lond. 459 (2003) 2347.
[75] G.Z. Voyiadjis, F.H. Abed, Mech. Mater. 37 (2005) 355.

[76] J.W. Hutchinson, K.W. Neale, Acta Metall. 25 (1977) 839.
[77] F. Li, Scripta Metall. Mater. 32 (1995) 463.
[78] H.J. Zhang, W.D. Wen, H.T. Cui, Mater. Sci. Eng. A 504 (2009) 99.
[79] G.A. Alers, Phys. Rev. 119 (1960) 1532.
[80] P.S. Branício, J.P. Rino, Phys. Rev. B 62 (2000) 16950.
[81] T.W. Wright, K.T. Ramesh, Int. J. Impact Eng. 36 (2009) 1242.
[82] J. Li, Modell. Simul. Mater. Sci. Eng. 11 (2003) 173.
[83] C.L. Kelchner, S.J. Plimpton, J.C. Hamilton, Phys. Rev. B 58 (1998) 11085.
[84] H. Tsuzuki, P.S. Branicio, J.P. Rino, Comput. Phys. Commun. 177 (2007) 518.
[85] V.V. Bulatov, W.G. Wolfer, M. Kumar, Scripta Mater. 63 (2010) 144.
[86] E.M. Bringa, V.A. Lubarda, M.A. Meyers, Scripta Mater. 63 (2010) 148.
[87] M.A. Tschopp, D.E. Spearot, D.L. McDowell, Modell. Simul. Mater. Sci. Eng. 15 (2007) 693.
[88] G.I. Kanel, S.V. Razorenov, A.V. Utkin, V.E. Fortov, K. Baumung, H.U. Karow, D. Rusch, V. Licht, J. Appl. Phys. 74 (1993) 7162.
[89] V. Tvergaard, Adv. Appl. Mech. 27 (1990) 83.
[90] J.F. Alder, V.A. Phillips, J. Instrum. Met. 83 (1954) 80.
[91] J.P. Chang, W. Cai, V.V. Bulatov, S. Yip, Mater. Sci. Eng. A 309 (2001) 160.
[92] R. Hill, The Mathematical Theory of Plasticity, Clarendon Press, Oxford, 1950.
[93] C.N. Reid, Acta Metall. 14 (1968) 13.